



Photo-controlled degradation of PLGA/Ti₃C₂ hybrid coating on Mg-Sr alloy using near infrared light

Li Liu^a, Bo Huang^a, Xiangmei Liu^{a,*}, Wei Yuan^b, Yufeng Zheng^{b,**}, Zhaoyang Li^c, Kelvin Wai Kwok Yeung^d, Shengli Zhu^c, Yanqin Liang^c, Zhenduo Cui^c, Shuilin Wu^{c,***}

^a Hubei Key Laboratory of Polymer Materials, Ministry-of-Education Key Laboratory for the Green Preparation and Application of Functional Materials, School of Materials Science & Engineering, Hubei University, Wuhan, 430062, China

^b State Key Laboratory for Turbulence and Complex System and Department of Materials Science and Engineering, College of Engineering, Peking University, Beijing, 100871, China

^c The Key Laboratory of Advanced Ceramics and Machining Technology by the Ministry of Education of China, School of Materials Science & Engineering, Tianjin University, Tianjin, 300072, China

^d Department of Orthopaedics & Traumatology, Li Ka Shing Faculty of Medicine, The University of Hong Kong, Pokfulam, Hong Kong, 999077, China

ARTICLE INFO

Keywords:
Magnesium
Ti₃C₂ MXene
Coating
Photoresponsive
Degradation

ABSTRACT

A PLGA/Ti₃C₂ hybrid coating was successfully deposited on the surface of magnesium-strontium (Mg-Sr) alloys. Compared with the corrosion current density (i_{corr}) of the Mg-Sr alloy (7.13×10^{-5} A/cm²), the modified samples (Mg/PLGA/Ti₃C₂) was lower by approximately four orders of magnitude (7.65×10^{-9} A/cm²). After near infrared 808 nm laser irradiation, the i_{corr} of the modified samples increased to 3.48×10^{-7} A/cm². The mechanism is that the local hyperthermia induced the free volume expansion of PLGA, and the increase in intermolecular gap enhanced the penetration of electrolytes. Meanwhile, the cytotoxicity study showed that the hybrid coating endowed the Mg-Sr alloy with enhanced biocompatibility.

1. Introduction

In the past decades, magnesium (Mg) and its alloys have received extensive attention for their application in artificial implants because they exhibit such advantages as remarkable mechanical properties, biocompatibility, and degradability [1–5]. Comparing with traditional implantable materials (e.g. titanium alloys, stainless steels, and other metallic materials), the Young's modulus of the Mg-based alloys was 41–45 GPa, similar to a natural bone (10–30 GPa) [6,7]. In addition, the excellent biocompatibility and the natural degradation of Mg-based alloys in human physiological environment can effectively prevent the damage of secondary surgery [7,8]. With the development of medicine and materials science, it is expected that implant materials can be degraded and absorbed gradually with the regeneration of tissues or organs after the completion of medical functions [2]. Strontium (Sr) is an essential trace element for human body, and 99% of Sr is stored in the bones [9]. Sr promotes the growth of osteoblasts and the synthesis of collagen, and it effectively prevents bone resorption [10–12]. As an

alloy element, Sr exerts a strong grain-refining for Mg alloys [12–15]. Studies suggested that Sr significantly enhanced the anti-corrosion capability of Mg alloys by improving their surface performance relative to that of pure Mg [9,12].

Mg-based alloys exhibit uncontrollable rapid corrosion when used as temporary implant materials, it is a serious problem on account of the chemical properties of Mg [16–18]. Moreover, such phenomenon signifies that Mg-based alloys will lose their expected inherent function. The rapid and uncontrollable corrosion rate of Mg-based alloys leads to hydrogen evolution and high local alkalization, which tend to cause great challenges in tissue reconstruction [19–21]. Thus, controlling the degradation rate of the Mg-based alloys is essential in their clinical application.

Many strategies have been performed to regulate the anti-corrosion performance of Mg-based alloys; these strategies include structure design [22,23], surface modification [24–28], and metallurgical alloying [29,30]. For example, an increased cooling rate of an alloy improves the grain refinement in and the formation of α -Mg phase, hence

Peer review under responsibility of KeAi Communications Co., Ltd.

* Corresponding author.

** Corresponding author.

*** Corresponding author.

E-mail addresses: liuxiangmei1978@163.com (X. Liu), yfzheng@pku.edu.cn (Y. Zheng), shuilinwu@tju.edu.cn (S. Wu).

<https://doi.org/10.1016/j.bioactmat.2020.08.013>

Received 27 July 2020; Received in revised form 16 August 2020; Accepted 16 August 2020

Available online 15 September 2020

2452-199X/ © 2020 The Authors. Publishing services by Elsevier B.V. on behalf of KeAi Communications Co., Ltd. This is an open access article under the CC BY-NC-ND license (<http://creativecommons.org/licenses/by-nc-nd/4.0/>).

enhance the anti-corrosion performance of the alloy [31]. Qi et al. [32] confirmed that a gelatin nanosphere/chitosan with simvastatin-loaded composite coating could increase the anti-corrosion performance and osteoinductivity of WE43 alloy. Moreover, the addition of different amounts of elemental calcium improves the ultimate tensile strength and decreases the corrosion rate of Mg-based alloys [30]. However, as an implant material, Mg-based alloys must have a controllable degradation rate as well as a good corrosion resistance.

Being a new two-dimensional material, MXene has been receiving widespread attention since its discovery by Gogotsi and Barsoum due to its surface activity and metallic conductivity [33–36]. MXenes include a large group of carbonitrides and transition metal carbides, which can be obtained by selectively extracting layers from the MAX phases. Ti_3C_2 MXene has been attracting great attention for its application in photothermal therapy [37,38], biosensors [39], and antibacterial agents [40] due to its excellent near infrared (NIR) absorption ability and biosafety. Similar to Ti_3C_2 MXene, the poly(lactic-co-glycolic acid) (PLGA) has been widely used in biomedical applications due to it has good biocompatibility, non-toxicity, good film-forming properties and good biodegradability, furthermore, it is approved by the Food and Drug Administration [41–43]. Earlier studies reported that the anti-corrosion performance of Mg-Zn alloy was improved through coating with PLGA [44].

We describe herein a PLGA/ Ti_3C_2 hybrid coating that is used to adjust the degradation rates of Mg-Sr alloy through 808 nm NIR light irradiation. In this work, the coating combines of the advantages of both PLGA and Ti_3C_2 when they are tightly combinative, PLGA improves the overall biocompatibility of the alloy and reduces the contact between the magnesium substrate and the liquid environment. Meanwhile, Ti_3C_2 endows the alloy good photothermal effect. Expectedly, the Ti_3C_2 nanosheets endowed the hybrid coating with high NIR absorption and photothermal properties, thus amplifying the intermolecular gap in PLGA through local hyperthermia. *In vitro* cytotoxicity assay results showed that the alloys coated with PLGA/ Ti_3C_2 hybrid coating demonstrated a higher biocompatibility than the pure Mg-Sr alloys and provide possibility of more application of magnesium implants.

2. Materials and method

2.1. Material preparation

The substrates of the Mg-1Sr alloy was fabricated as described previously [45]. In the current work, Mg-1Sr alloys with $\Phi 10 \times 5$ mm dimensions were selected as the substrates, which were washed with acetone (purity $\geq 99.5\%$, Sinopharm Chemical Reagent Co.,Ltd, China) ultrasonically for 15min. Then, the substrates were ground with SiC paper (the final size was 1200-grit) and then washed with ethanol (purity $\geq 99.7\%$, Sinopharm Chemical Reagent Co.,Ltd, China) ultrasonically for 15min. Finally, the samples were dried and stored at vacuum drying oven at 25 °C and the for subsequent use.

2.2. Synthesis of Ti_3C_2 nanosheets

First, 2.0 g Ti_3AlC_2 powder was slowly placed in 20 mL 20% HF (Sinopharm Chemical Reagent Co.,Ltd, China) aqueous solution; the mixture was allowed to stand for 12 h. After etching, clay-like solid materials were recycled by centrifugation and then washed by deionized water (conductivity = 5.5 $\mu\text{S}/\text{cm}$) and ethanol for three times. The etched Ti_3C_2 nanosheets were dispersed in 15 mL DMSO (purity $\geq 99.5\%$, Sinopharm Chemical Reagent Co.,Ltd, China) and stirred continuously for 24 h. The suspension was re-dispersed under sonication for 8 h. Subsequently, the Ti_3C_2 nanosheets were cleaned with deionized water and ethanol and then collected by centrifugation (Scheme 1a).

2.3. Preparation of the PLGA/ Ti_3C_2 hybrid coating

The PLGA/ Ti_3C_2 hybrid coating was prepared by using a simple and environment-friendly solution casting method. Typically, a 5% (w/v) PLGA precursor solution was prepared by dissolving PLGA particles ($M_w = 120000$; co-polymer ratio = 85:15; viscosity = 0.61) in dichloromethane (purity $\geq 99.5\%$, Sinopharm Chemical Reagent Co.,Ltd, China). Ti_3C_2 nanosheets were added into the as-prepared PLGA precursor solution; the concentration of this solution was 12.5 mg/mL. The solution was subsequently dispersed by ultrasound for 30 min. Finally, 40 μL of the solution was used to coat the surface of Mg through a casting method, and the solution casting process was repeated (Scheme 1b). The pure Mg-1Sr alloy (Mg) served as the control; the sample modified with PLGA precursor solution was denoted as Mg/PLGA, whereas that modified with the PLGA- Ti_3C_2 mixture was named Mg/PLGA/ Ti_3C_2 . The Mg, Mg/PLGA, and Mg/PLGA/ Ti_3C_2 samples irradiated with NIR were denoted as Mg(L), Mg/PLGA(L), and Mg/PLGA/ Ti_3C_2 (L), respectively. The samples were stored under spotless and arid conditions for subsequent experiments.

2.4. Characterization

The structure of Ti_3C_2 was examined using field emission scanning electron microscopy (FE-SEM, ZEISS Sigma 500, GER), transmission electron microscopy (TEM, Tecnai G20 electron microscope, FEI, USA), whereas the phase of Ti_3C_2 was examined using X-ray diffraction (XRD, D8A25, Bruker, GER). The microscopic morphology and chemical compositions were examined by scanning electron microscopy (SEM, JSM-6510LV, JP). A spectrophotometer (UV-3600, Shimadzu, JP) was used to obtain the UV-vis-NIR absorption spectra. The chemical bonds of the coatings were measured by Fourier transform infrared spectroscopy (FT-IR) (Nicolet 570, USA). The chemical states were determined by X-ray photoelectron spectroscopy (XPS) (Thermo Fisher Scientific Escalab 250Xi, USA) with Al K α irradiation.

2.5. Contact angle

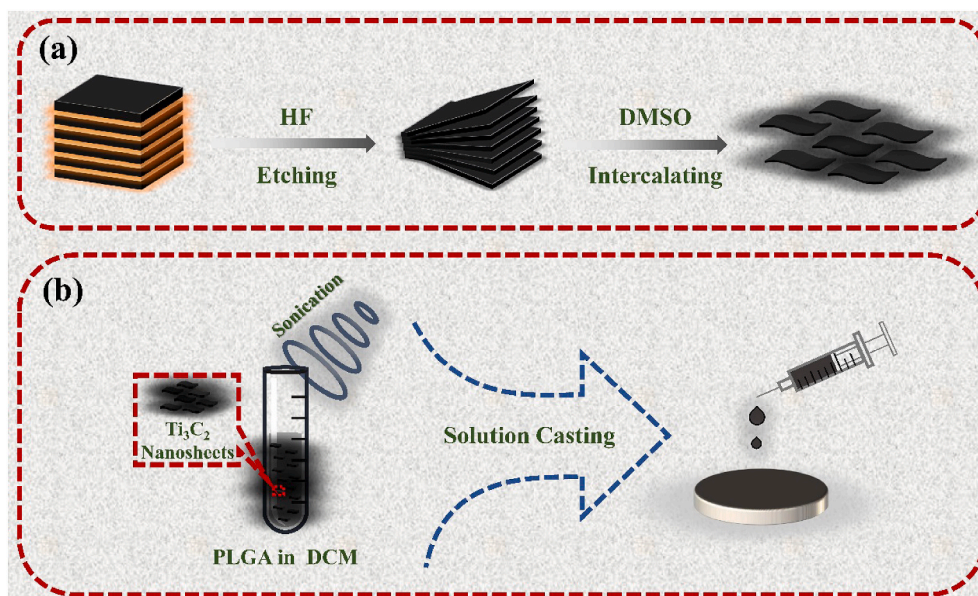
The water contact angles of the different samples were determined by a contact angle meter (Powereach JC2000D1 Zhong-Cheng Digital, China) at room temperature. Deionized water (5 μL) was placed on the surface of the samples, and their contact angles were recorded by an optical microscope. All tests were performed three times to obtain an average value.

2.6. Photothermal performance of the PLGA/ Ti_3C_2 coating

The photothermal performance of the samples irradiated with 808 nm NIR laser was measured and recorded by an infrared imaging device (Testo 875-1i). The three groups (Mg, Mg/PLGA, and Mg/PLGA/ Ti_3C_2) were put in a 24-well plates containing 1 mL simulated body fluid (SBF) and irradiated by 808 nm NIR laser for 20 min (1.0 W cm^{-2}). The infrared thermal images were obtained by the infrared imaging device every 2 min.

2.7. Electrochemical measurements

A CHI660E electrochemical analyzer was selected to measure the anti-corrosion performance of the samples in SBF at ambient temperature and a stable open circuit potential. A three-electrode device was adopted (i.e., with the sample as the working electrode, the platinum plate electrode and the saturated calomel electrode as the auxiliary electrode and reference electrode). The exposed area of the working electrode was 0.785 cm^2 . Electrochemical impedance spectroscopic (EIS) analysis was conducted at a sinusoidal potential of 5 mV and at a frequency range of 10^{-2} Hz to 10^5 Hz. The sweep rate for the potentiodynamic polarization curves was 2 mV/s. Each test was



Scheme 1. Schematic diagram of the preparation process of Ti_3C_2 nanosheets and PLGA/ Ti_3C_2 hybrid coating.

conducted using three parallel samples to improve the statistics. The results were analyzed by the Zsimpwin 3.21 software.

2.8. Immersion tests

The samples were immersed in SBF at 37 ± 0.5 °C for 14 days to determine their long-term degradation behavior. The ratio of the immersion solution volume (mL) to the samples' test area (cm^2) was 30:1, and three parallel measurements were conducted for each group. The pH values were monitored at 0, 2, 4, 6, 12, and 24 h in the first day, and then measured at 24 h intervals. The degradation rates of the alloy samples were determined based on pH values.

2.9. In vitro cytotoxicity assay

2.9.1. Cell viability

Osteoblasts (MC3T3-E1) were selected for the *in vitro* research. The MC3T3-E1 cells were maintained in a cell culture flask (Nest) containing Dulbecco's Modified Eagle Medium (DMEM, high glucose, Gibco) with 10% fetal bovine serum and 1% penicillin–streptomycin at 37 °C under 5% CO_2 . The culture medium was changed with fresh medium every 48 h, and the cells were digested with 0.25% trypsin-EDTA solution (Gibco).

The samples were sterilized by exposing them to UV radiation for 30 min and then incubated in culture medium for 24 h. The ratio of the extraction medium's volume to the sample's surface area was 1.25 mL cm^{-2} . The extracted solution was used as the culture medium for the subsequent experiments. The cells with a density of 5×10^4 cells/well were injected into 96-well plates for cell viability detection. After incubation for 24 h, the extracted solution was used to replace the culture medium. As described previously [45], the viability of the cells that were cultured for 1, 3, and 5 days was measured by standard MTT assay.

2.9.2. Cell morphologies

The cells (5×10^4 cells/well) were placed in 24-well plates and then cultured for 12 h. After removing the culture medium, the samples were washed three times with phosphate buffered solution (pH = 7.4) and then soaked in 4% formaldehyde (Sinopharm Chemical Reagent Co., China) solution for 10 min to fix the cells on the samples at room temperature. The F-actin of the cells was stained with TRITC Phalloidin

(Yeasen, Shanghai), and their nuclei were dyed with 4,6-diamidino-2-phenylindole dihydrochloride (Yeasen, Shanghai). The corresponding morphologies of the samples were observed using an inverted fluorescence microscope (Olympus, IX73).

2.10. Statistical analysis

All the repeated data were evaluated as mean \pm standard deviation, and the one-way ANOVA was used to determine the statistical significance. P values of less than 0.05 indicated statistical significance.

3. Results and discussion

3.1. Characterization of the surface coating

The as-received Ti_3AlC_2 powder had a close-packed bulk structure (Fig. 1a and Fig. S1a). Following etching in HF aqueous solution, the Al^{3+} ions were removed as shown in the following reaction [34]:



The FE-SEM image shows that the etched Ti_3C_2 powder exhibited a stacked flake-like structure (Fig. 1b). Furthermore, the TEM image (Fig. 1c) reveals that the Ti_3C_2 nanosheets, which were approximately 200 nm thick, could be obtained by intercalation with DMSO. The XRD patterns confirmed the formation of Ti_3C_2 nanosheets. Compared with the intense peak of Ti_3AlC_2 powder, that of the Ti_3C_2 nanosheets was obviously lower ($2\theta \approx 39^\circ$). This result is consistent with a previous finding [40]. After delamination, a new characteristic peak ($2\theta \approx 8^\circ$) appeared due to the presence of the Ti_3C_2 nanosheets, and the basal reflections 002 and 006 became more obvious (Fig. 1d). As reported, strengthened 002, 0010 diffractions are related to the stacking of monolayer Ti_3C_2 nanosheets [38]. This finding further confirms that the Ti_3C_2 nanosheets were obtained through etching and solvent intercalation.

The microscopic morphology of the modified samples was observed by SEM. Fig. 1e shows the presence of an apparent scratch on the mechanically polished Mg substrate. The tip of the scratch was curled as seen under high magnification (Fig. S1b). The scratch obviously disappeared after coating with PLGA, and the surface of the resulting Mg/PLGA is smooth (Fig. 1f). Fig. S1c shows more details of the surface morphology of the Mg/PLGA. A faint reticular trace of Mg/PLGA could

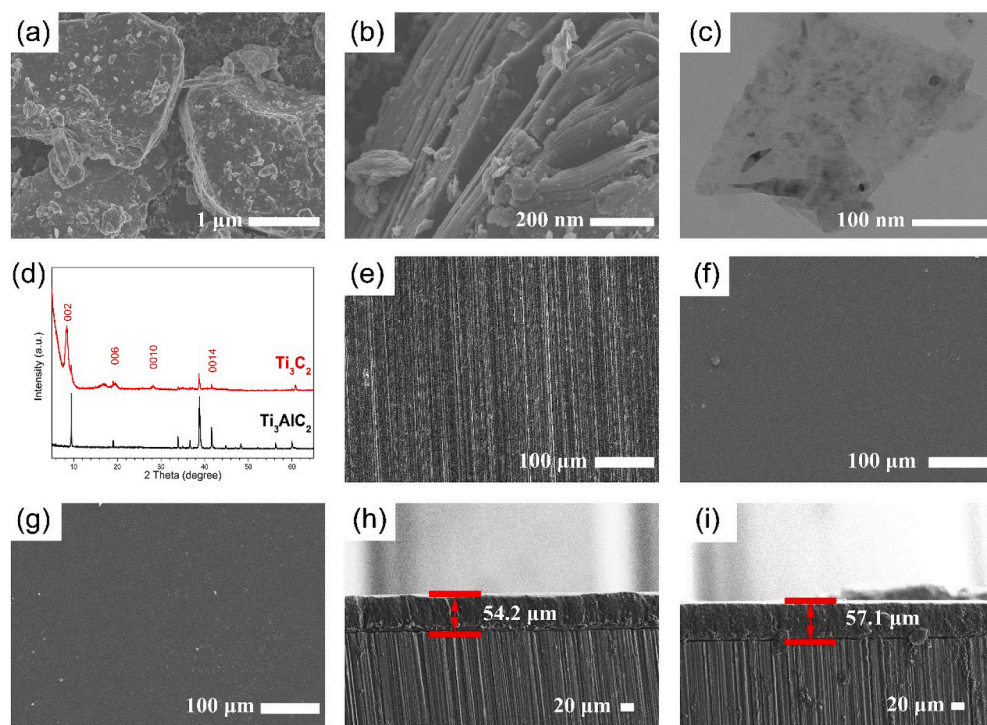


Fig. 1. Characterization of Ti_3C_2 nanostructure and surface coating: (a) FE-SEM image of bulk Ti_3AlC_2 ; (b) FE-SEM image of layered Ti_3C_2 ; (c) TEM image of delaminated Ti_3C_2 nanosheets; (d) XRD patterns of raw Ti_3AlC_2 and Ti_3C_2 after delamination. Surface morphologies: (e) Mg; (f) Mg/PLGA; (g) Mg/PLGA/ Ti_3C_2 ; (h), Cross-section morphologies of (f); (i) Cross-section morphologies of (g).

be observed due to solvent volatilization during the coating process. Unlike the Mg/PLGA, the Mg/PLGA/ Ti_3C_2 not only had a smoother surface; its reticular trace also disappeared (Figs. 1g and S1d). The Mg/PLGA and Mg/PLGA/ Ti_3C_2 were approximately 54.2 and 57.1 μm thick, respectively, as seen in their cross-sectional images (Fig. 1h, i and Fig. S2). As shown in Table 1S, the disappearance of aluminum element confirmed the successful preparation of Ti_3C_2 from the Ti_3AlC_2 powder through HF etching. Meanwhile, after modification with a PLGA or PLGA/ Ti_3C_2 hybrid coating, the Mg content significantly decreased, indicating that the hybrid coating could effectively cover the substrates. Furthermore, elemental mapping of C and Ti in the Mg/PLGA/ Ti_3C_2 approved that the Ti_3C_2 particles were uniformly dispersed in PLGA.

FT-IR and XPS were used to approve the existence of PLGA and Ti_3C_2 nanosheets, respectively, in the hybrid coating. According to Fig. 2a, the characteristic peak at 1758 cm^{-1} is regarded as the C=O stretching of the COO^- group, and the peaks at 1182, 1127, and 1086 cm^{-1} are related to the C–O group [44,45]. The characteristic absorption peaks were consistent with PLGA, suggesting that PLGA was

successfully fabricated on the samples. As shown in Fig. 2b, the order of intensity of the peak of C 1s at approximately 284.5 eV is as follows: Mg/PLGA/ Ti_3C_2 > Mg/PLGA > Mg, which is related to the presence of PLGA and Ti_3C_2 nanosheets. This result is consistent with the previous findings [34,39], indicating that Ti_3C_2 nanosheets exist in Mg/PLGA/ Ti_3C_2 . Meanwhile, the signal of Mg 2p significantly decreased, further confirming the effective encapsulation of the surface by the hybrid coating.

Compared with Mg and Mg/PLGA, Mg/PLGA/ Ti_3C_2 showed a broader and stronger optical absorption from UV to NIR region (Fig. 3a), demonstrating that the presence of Ti_3C_2 nanosheets significantly enhanced the light absorption capacity of the hybrid coating. Differential scanning calorimetry (DSC) was used to test the glass transition temperature (T_g) of PLGA. The DSC thermogram (Fig. 3b) revealed that the T_g value of PLGA was approximately $48.5\text{ }^\circ\text{C}$. This finding indicates that the PLGA/ Ti_3C_2 hybrid coating would have a larger hole due to the free volume expansion of PLGA when the temperature exceeded $48.5\text{ }^\circ\text{C}$ [44]. Moreover, the increase in

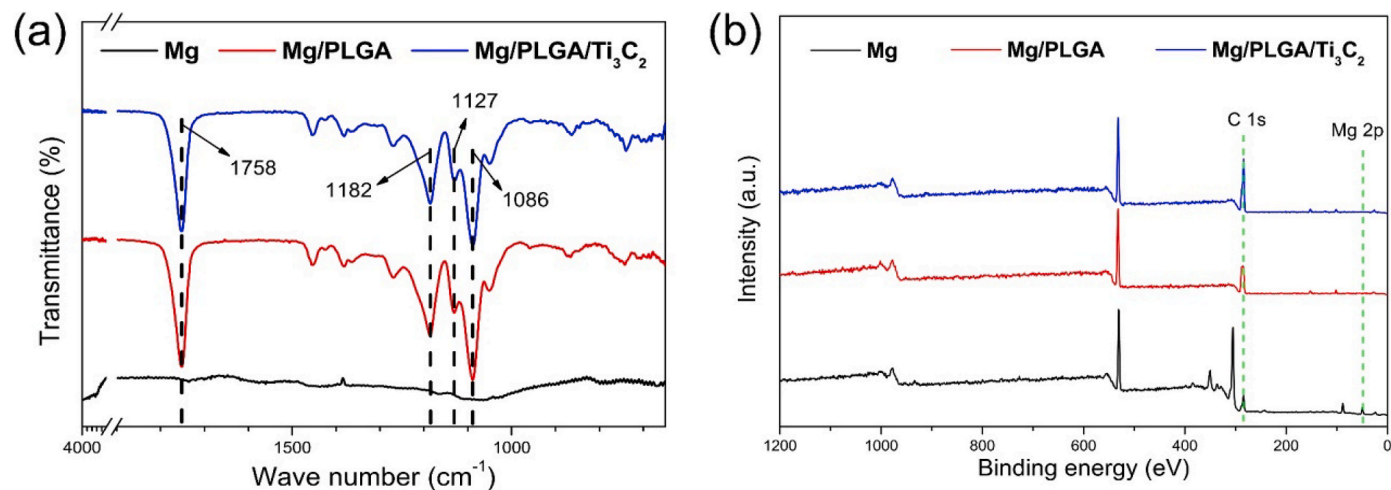


Fig. 2. (a) FT-IR spectra, and (b) XPS spectra of the Mg, Mg/PLGA, Mg/PLGA/ Ti_3C_2 .

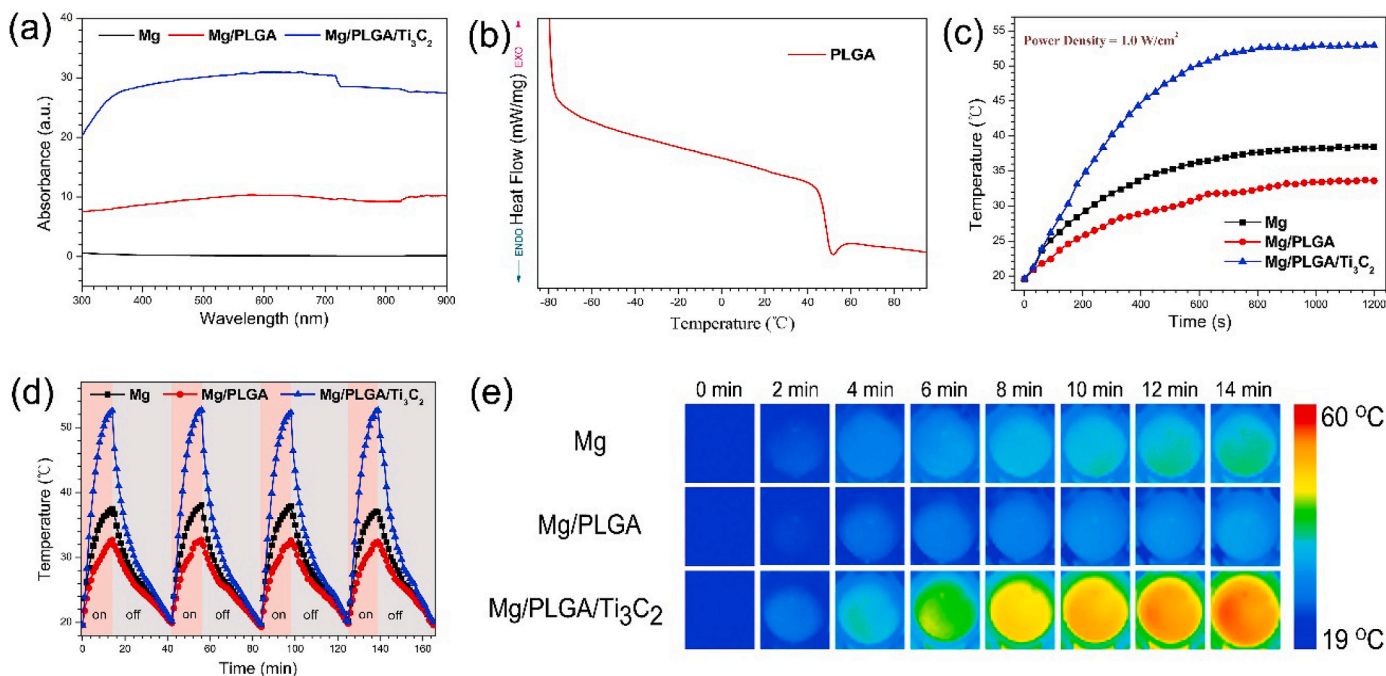


Fig. 3. Photothermal properties measurements under NIR 808 nm laser irradiation: (a) UV-vis-NIR absorption spectra of the different modified samples; (b) Differential scanning calorimetry (DSC) analysis of PLGA; (c) Photothermal heating curves of Mg, Mg/PLGA and Mg/PLGA/Ti₃C₂ (1.0 W/cm², 20 min); (d) Temperature variations of the different modified samples for 4 cycles; (e) Real-time infrared thermal images of different samples immersed into SBF under continuous 808 nm laser irradiation for 14 min.

intermolecular gap weakened the anti-electrolyte permeability property of the coating [47].

The photothermal properties of the samples were explored based on the photothermal heating curves and photothermal images obtained under NIR laser irradiation at 808 nm (1.0 W cm⁻²). As shown in Fig. 3c, after irradiation with 808 nm NIR laser for 20 min, the final temperatures of Mg and Mg/PLGA were approximately 38.4 °C and 33.5 °C, respectively. As for Mg/PLGA/Ti₃C₂, the final temperature reached up to approximately 52.1 °C. Compared with Mg and Mg/PLGA, Mg/PLGA/Ti₃C₂ demonstrated a more excellent photothermal performance, and its maximum temperature exceeded the T_g of the PLGA. The Ti₃C₂ nanosheets endowed the Mg/PLGA/Ti₃C₂ with improved NIR light absorption properties and a more remarkable photothermal conversion efficiency. According to Fig. 3d, the temperature variations with NIR 808 nm laser irradiation for 4 cycles displayed that there were a stable on-off and photothermal effect.

Fig. 3e shows the real-time infrared thermal pictures of the different samples during the 808 nm NIR laser irradiation. The decreasing order of the heating rates of the samples is as follows: Mg/PLGA/Ti₃C₂ > Mg > Mg/PLGA. The PLGA/Ti₃C₂ hybrid coating demonstrated the strongest photothermal effect and thus is an optimal candidate for the light-controlled degradation of Mg alloys.

3.2. Electrochemical tests

The corrosion behavior of Mg alloys *in vivo* is considered as an electrochemical corrosion process [21,23]. So, the anti-corrosion performance of the treated samples was measured using potentiodynamic polarization curves and EIS. The potentiodynamic polarization curves of Mg, Mg(L), Mg/PLGA, Mg/PLGA(L), Mg/PLGA/Ti₃C₂, and Mg/PLGA/Ti₃C₂(L) are shown in Fig. 4. As indicated from the parameters of the free corrosion potentials (E_{corr}) and corrosion current density (i_{corr}) (Table 1), the i_{corr} of the Mg was 7.13×10^{-5} A/cm². After irradiation with 808 nm NIR laser, the i_{corr} value of Mg(L) was 7.63×10^{-5} A/cm², indicating that the irradiation did not significantly affect the anti-corrosion performance of the substrates. Furthermore, the i_{corr} values of

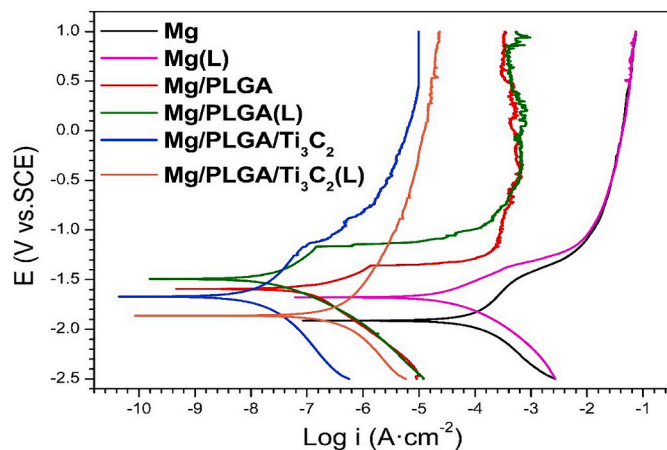


Fig. 4. Potentiodynamic polarization measurements results of each group.

Table 1

The results of free corrosion potentials E_{corr} and corrosion current densities i_{corr} .

	E_{corr} (V _{SCE})	i_{corr} (A/cm ²)
Mg	-1.909 ± 0.063	$(7.13 \pm 4.363)E-5$
Mg(L)	-1.688 ± 0.160	$(7.63 \pm 6.823)E-5$
Mg/PLGA	-1.649 ± 0.053	$(5.96 \pm 3.521)E-8$
Mg/PLGA(L)	-1.733 ± 0.133	$(3.36 \pm 1.609)E-8$
Mg/PLGA/Ti ₃ C ₂	-1.701 ± 0.054	$(7.65 \pm 7.620)E-9$
Mg/PLGA/Ti ₃ C ₂ (L)	-1.706 ± 0.133	$(3.48 \pm 1.999)E-7$

Mg/PLGA and Mg/PLGA(L) were 5.96×10^{-8} and 3.36×10^{-8} A/cm², respectively. These values are lower by approximately three orders of magnitude than that of Mg, indicating that modification with PLGA enhanced the anti-corrosion performance of the Mg-Sr alloy substrates. Moreover, the 808 nm NIR laser irradiation did not weaken the Mg/PLGA's anti-corrosion performance, which remained similar to that of Mg. The i_{corr} value of Mg/PLGA/Ti₃C₂ was only 7.65×10^{-9} A/cm²,

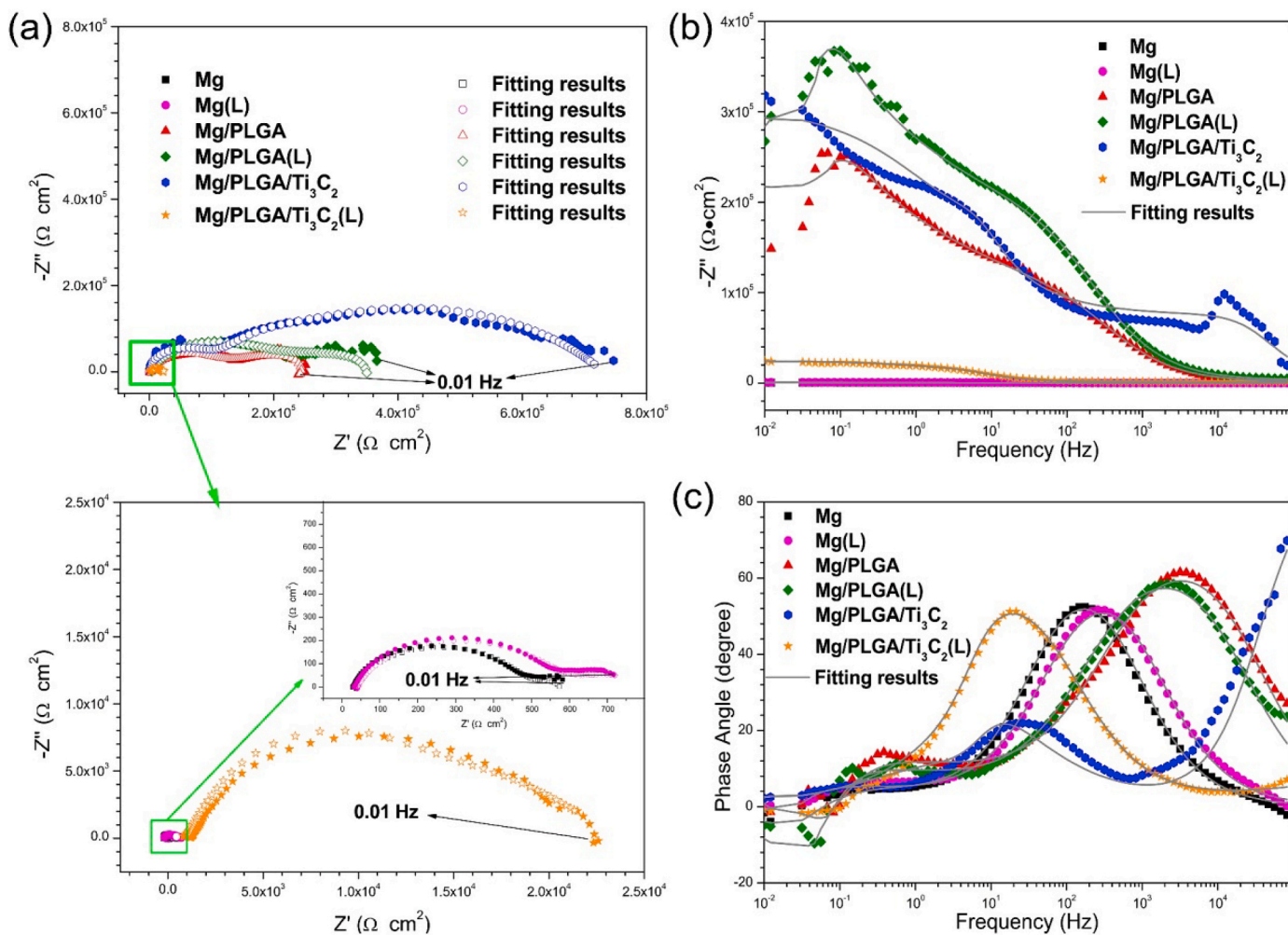


Fig. 5. EIS diagrams of different modified samples: (a) Nyquist plots; (b) and (c) Bode plots.

which is lower than that of Mg by approximately four orders of magnitude, demonstrating a considerable improvement in corrosion resistance of the former. Compared with the i_{corr} values of Mg(L) and Mg/PLGA(L), that of Mg/PLGA/Ti₃C₂(L) that was exposed to 808 nm NIR laser for 20 min significantly increased (3.48×10^{-7} A/cm²). Overall, the PLGA/Ti₃C₂ hybrid coating endowed the Mg-Sr alloy substrates with excellent corrosion resistance. Furthermore, unlike the traditional corrosion-resistant coating, the PLGA/Ti₃C₂ hybrid coating not only could impart a remarkable anti-corrosion property to the substrates but could also control the corrosion rates through NIR laser irradiation at 808 nm.

The EIS method is usually used to study the electrochemical corrosion kinetics and to evaluate the anti-corrosion performance of metal-based materials. The capacitive loop in the middle- and high-frequency regions and the induction loop in the low-frequency region of the samples could be clearly observed in the Nyquist plots (Fig. 5a). The Pébère model revealed that the middle-frequency capacitive loop is related to the mass transfer of Mg²⁺, and the inductive loop corresponds to the absorption of Mg⁺ on the surface [48]. The decreasing order of the diameter of the samples' capacitive loops is as follows: Mg/PLGA/Ti₃C₂ > Mg/PLGA(L) > Mg/PLGA > Mg/PLGA/Ti₃C₂(L) > Mg(L) > Mg. The impedance modulus ($|Z|_{f \rightarrow 0}$) also followed the pattern for the capacitive loop diameter (Fig. 5b). The $|Z|_{f \rightarrow 0}$ value of Mg/PLGA/Ti₃C₂ ($3.18 \times 10^5 \Omega \text{ cm}^2$) was greater than that of Mg ($4.93 \times 10^2 \Omega \text{ cm}^2$). Irradiation with 808 nm NIR laser significantly reduced the $|Z|_{f \rightarrow 0}$ value of Mg/PLGA/Ti₃C₂(L) to $2.46 \times 10^5 \Omega \text{ cm}^2$, further confirming that the PLGA/Ti₃C₂ hybrid coating could increase

the corrosion resistance of Mg-Sr alloys and that the anti-corrosion performance could be controlled by the 808 nm NIR laser. As shown in Fig. 5c, the phase angle of the modified samples is higher than that of Mg in the high-frequency region. This finding indicates that an anti-corrosion passivation film completely covered the surface of Mg [25].

The EC model was used to analyze the EIS data (Fig. 6). The fitting results are shown in Table 2, where R_s is regarded as the solution resistance of the SBF. A constant phase element is used to eliminate the influence of the inhomogeneity of the electrode's surface on the fitting process and to enhance the accuracy of the fitting results [21,45]. R_L and L represent the inductance resistance and inductance, respectively, and they are related to electrolyte penetration and to the dissolution and pitting corrosion of the Mg substrate. As for Mg and Mg(L), C_1 was

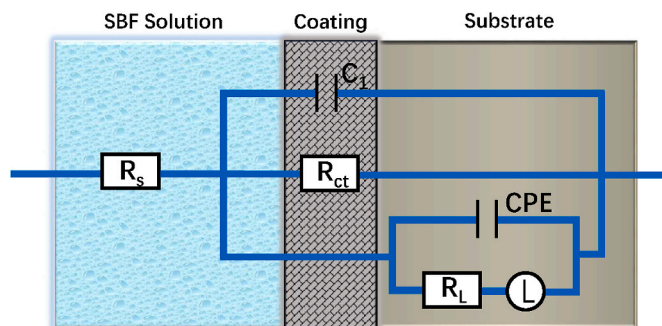


Fig. 6. The equivalent circuits of the EIS spectra, $R_s(C_1(R_{ct}(Q_{CPE}(R_L)L)))$.

Table 2

The fitting data of the EIS spectra of the different samples using equivalent circuits shown in Fig. 6.

	Mg	Mg(L)	Mg/PLGA	Mg/PLGA(L)	Mg/PLGA/Ti ₃ C ₂	Mg/PLGA/Ti ₃ C ₂ (L)
C ₁ (Ω ⁻¹ cm ⁻² S ⁻ⁿ)	(2.53 ± 0.07)E-5	(1.35 ± 0.05)E-5	(1.89 ± 0.28)E-8	(2.95 ± 0.05)E-6	(1.49 ± 0.66)E-10	(4.24 ± 0.44)E-6
R _{ct} (Ω·cm ²)	(3.13 ± 0.08)E2	(4.83 ± 0.05)E2	(8.16 ± 0.34)E4	(4.31 ± 0.45)E3	(9.84 ± 0.12)E4	(7.73 ± 1.61)E2
Q _{CPE} (Ω ⁻¹ cm ⁻² S ⁻ⁿ)	(1.07 ± 0.27)E-2	(5.72 ± 0.14)E-3	(6.33 ± 0.16)E-6	(1.17 ± 0.20)E-8	(1.10 ± 0.20)E-7	(4.61 ± 0.29)E-6
R ₁ (Ω·cm ²)	(60.79 ± 0.61)	(248.1 ± 0.23)	(2.01 ± 0.41)E5	(5.43 ± 0.10)E5	(6.32 ± 0.04)E5	(2.46 ± 0.06)E4
L (H·cm ²)	(8.63 ± 0.50)E2	(3.57 ± 0.30)E3	(6.93 ± 0.59)E6	(4.02 ± 0.14)E6	(4.73 ± 0.74)E2	(6.01 ± 0.18)E2

related to the electric double layer capacitance of the electrode, and R_{ct} was mainly derived from the corrosion products. Unlike in Mg and Mg(L), C₁ and R_{ct} represent the coating capacitance and resistance, respectively, in the substrates modified with PLGA/Ti₃C₂ hybrid coating. As shown in Table 2, compared with that of Mg, the R_{ct} of Mg/PLGA/Ti₃C₂ significantly increased from 3.13 × 10² Ω cm² to 9.84 × 10⁴ Ω cm², indicating that the PLGA/Ti₃C₂ hybrid coating could provide effective protection to the substrate. By contrast, the R_{ct} of Mg/PLGA/Ti₃C₂(L) decreased by approximately two orders of magnitude (from 9.84 × 10⁴ Ω cm² to 7.73 × 10² Ω cm²), confirming that irradiation with 808 nm NIR laser could control the anti-corrosion performance of the PLGA/Ti₃C₂ hybrid coating. The decreasing order of the R₁ values is as follows: Mg/PLGA/Ti₃C₂ > Mg/PLGA(L) > Mg/PLGA > Mg/PLGA/Ti₃C₂(L) > Mg(L) > Mg. The results are similar to the Nyquist plot results, further confirming that the PLGA/Ti₃C₂ hybrid coating could increase the corrosion resistance of the Mg substrate and that the 808 nm NIR laser could regulate the anti-corrosion performance of the hybrid coating.

The masonry wall-like structure of the PLGA/Ti₃C₂ hybrid coating and the high conductivity of the Ti₃C₂ nanosheets played an important role in corrosion inhibition. On one hand, the PLGA/Ti₃C₂ hybrid coating with the structure similar to masonry not only hindered the direct contact between the metal substrates and the electrolyte solution but also made the path for electrolyte infiltration more tortuous. The corrosion process was delayed by the weakened cathode reaction in the electrochemical corrosion process (Scheme 2). Moreover, the PLGA molecules embedded between Ti₃C₂ nanosheets helped to prevent the transport of chlorine ions, water molecules, and other invasive species [49,50]. On the other hand, the high conductivity of the Ti₃C₂ nanosheets provided an alternative route for electron transfer during the corrosion process. Usually, corrosion begins at the interface between

metal substrates and their coating, and the electrons produced by the anodic reaction (metal oxidation) are transferred to the cathode position through the substrate to be reduced, completing the corrosion process. However, when the coating exhibits excellent conductivity, it brings an alternative path for electron transmission, so that the electrons produced in the anodizing process could not easily reach the cathodic reaction site, further reducing the electrochemical corrosion efficiency.

3.3. In vitro degradation behavior

Theoretically, during the process of immersion testing, the main chemical reaction is expressed as follows:

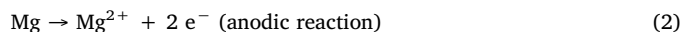
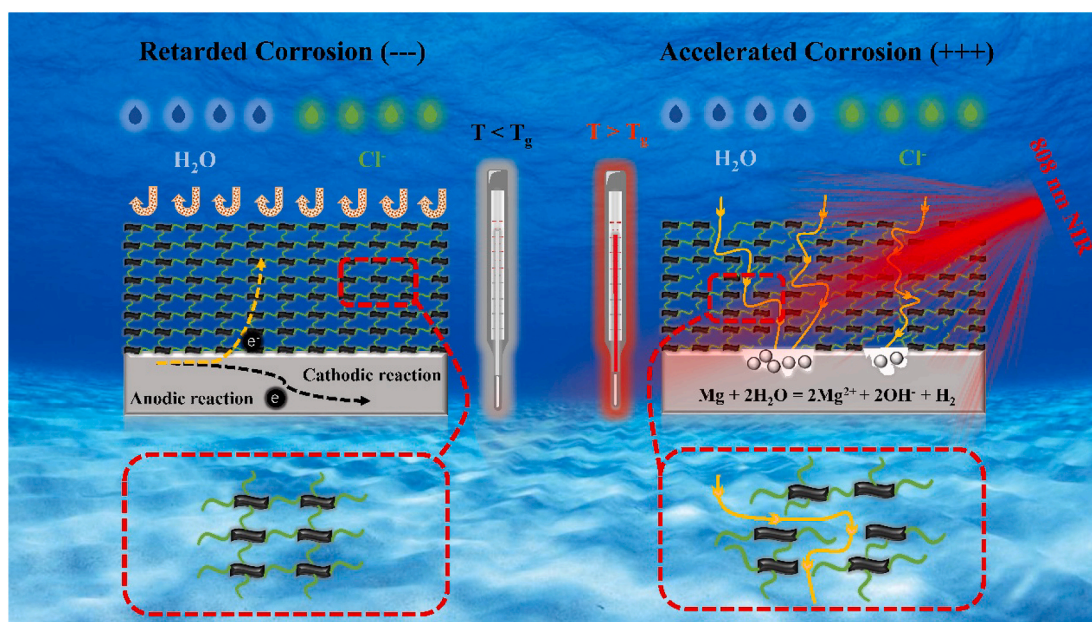


Fig. 7 shown 7.4–8.98 (Mg), 7.4–9.09 (Mg(L)), 7.4–7.73 (Mg/PLGA), 7.4–7.66 (Mg/PLGA(L)), 7.4–7.64 (Mg/PLGA/Ti₃C₂), and 7.4–8.16 (Mg/PLGA/Ti₃C₂(L)) pH ranges. According to Fig. 7a, the pH values of the Mg and Mg(L) samples were always higher than those of the other samples, and they maintained the maximum rate of rise. During the entire immersion process, no significant difference in pH was observed between Mg and Mg(L). Furthermore, the pH values for Mg/PLGA, Mg/PLGA(L), and Mg/PLGA/Ti₃C₂ maintained a low rate of rise and a small rising amplitude. At the end of the immersion measurements, the Mg/PLGA/Ti₃C₂ showed the lowest pH value (7.64). As for Mg/PLGA/Ti₃C₂(L), the pH only slightly changed at the beginning of the immersion (Fig. 7b). After immersion for 48 h, a slight increase in the rate of rise was observed, and the rate remained between that for Mg and Mg/PLGA/Ti₃C₂. Overall, the changes in pH values in SBF at



Scheme 2. Schematic of the degradation mechanism of the magnesium substrates.

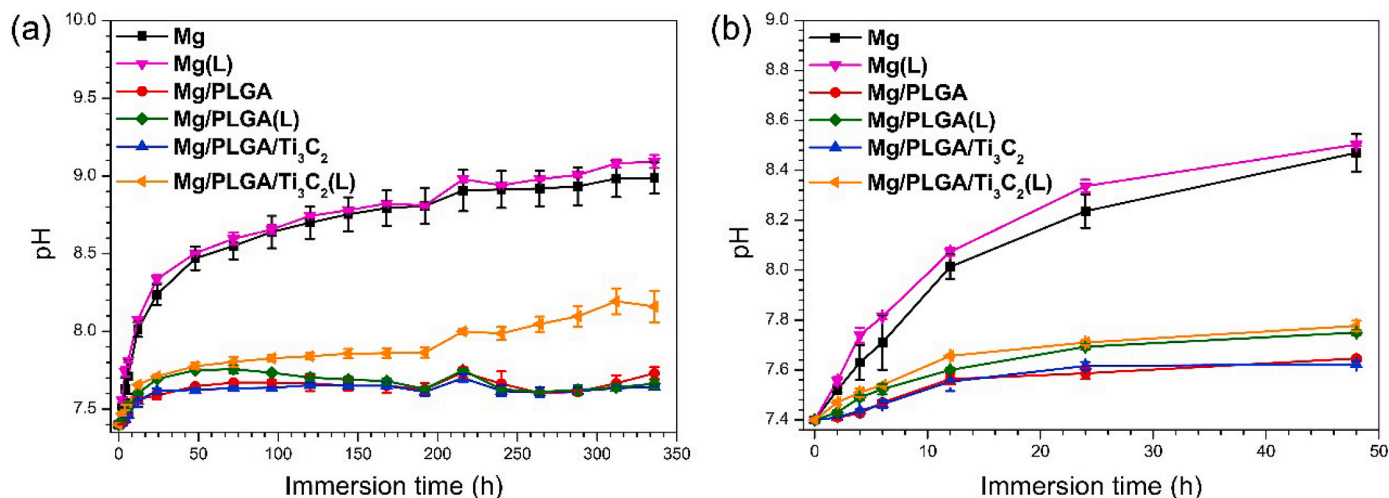


Fig. 7. The pH values evolution of the immersion medium over a period of 14 days.

37 °C confirmed that pretreatment with PLGA/Ti₃C₂ could effectively reduce the degradation rates of the Mg-Sr alloys. Moreover, the degradation rates of Mg/PLGA/Ti₃C₂ could be adjusted through 808 nm NIR laser irradiation. These results are consistent with the electrochemical test results.

Fig. 8 shows the details of the sample's morphology immersed in SBF for 14 days. During immersion, the modified samples displayed varying degrees of corrosion due to their diverse corrosion resistance. After 14 days of immersion, Mg was seriously corroded (Fig. 8a). The magnified schematic diagram (inset) shows the irregular crack-doped concave and convex morphologies of the surface of Mg. Meanwhile, Fig. S3a shown severe longitudinal pitting of the Mg substrates (marked with a red dotted line). After irradiation with NIR at 808 nm, Mg(L) was seriously corroded (Fig. 8b and Fig. S3b). The high magnification image (inset) and the cross-section morphology of Mg(L) was similar to that of Mg. Compared with the coating of Mg and Mg(L), that of Mg/PLGA remained intact and showed no obvious corrosion traces (Fig. 8c and Fig. S3c). Moreover, the magnified diagram of Mg/PLGA shows a slightly heave structure. As demonstrated in Fig. 8d and Fig. S3d, the surface and cross-section morphologies of Mg/PLGA(L) was similar to that of Mg/PLGA at the end of the immersion. Compared with Mg/PLGA, Mg/PLGA/Ti₃C₂ displayed a more complete and a smoother surface structure (Fig. 8e). Furthermore, the cross-section morphology of Mg/PLGA/Ti₃C₂ confirmed that the Mg substrate in the presence of the PLGA/Ti₃C₂ coating still maintains a relatively complete interface. However, compared with the surface of Mg/PLGA(L), that of the Mg/

PLGA/Ti₃C₂(L) was seriously damaged, and granular corrosion products were observed on the exposed part of the substrate toward the end of the immersion (Fig. 8f). Meanwhile, the cross section (Fig. S3f) shown a degree of pitting at the interface between the coating and the substrate. At the same time, the adhesion of the coating to the substrate became worse, and there were more corrosion products at the interface. As for Mg, whether irradiated with NIR at 808 nm or not, this substrate was seriously corroded after the immersion. By contrast, when not irradiated, the samples coated with PLGA or PLGA/Ti₃C₂ presented an intact coating and thus were protected from corrosion. The PLGA/Ti₃C₂ hybrid coating demonstrated an enhanced corrosion resistance effect. However, compared with the coating of Mg/PLGA(L), that of Mg/PLGA/Ti₃C₂(L) was damaged, and the exposed parts of the substrate was corroded at the end of the immersion.

The immersion measurement results are attributed to the presence of the PLGA coating, which delayed the penetration of electrolyte, prevented the direct contact between electrolytes and the substrates, and delayed the corrosion of the substrate. Furthermore, the addition of Ti₃C₂ nanosheets endowed the coating with an enhanced anti-permeability property. The remarkable conductivity of Ti₃C₂ nanosheets was beneficial to impair the electrochemical corrosion efficiency of the substrate when the coating was complete. Compared with Mg and Mg/PLGA, Mg/PLGA/Ti₃C₂ exhibited outstanding photothermal properties. With the NIR laser irradiation at 808 nm, the temperature of the hybrid coating exceeded the T_g of PLGA. At this point, the increased movement of the polymer chains increased the free volume expansion of the

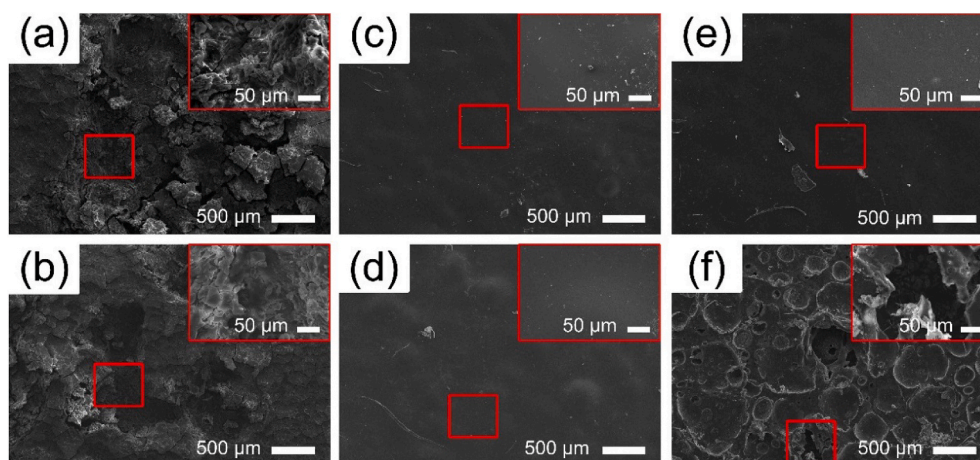


Fig. 8. Surface morphologies after immersion testing: (a) Mg; (b) Mg(L); (c) Mg/PLGA; (d) Mg/PLGA(L); (e) Mg/PLGA/Ti₃C₂; (f) Mg/PLGA/Ti₃C₂(L).

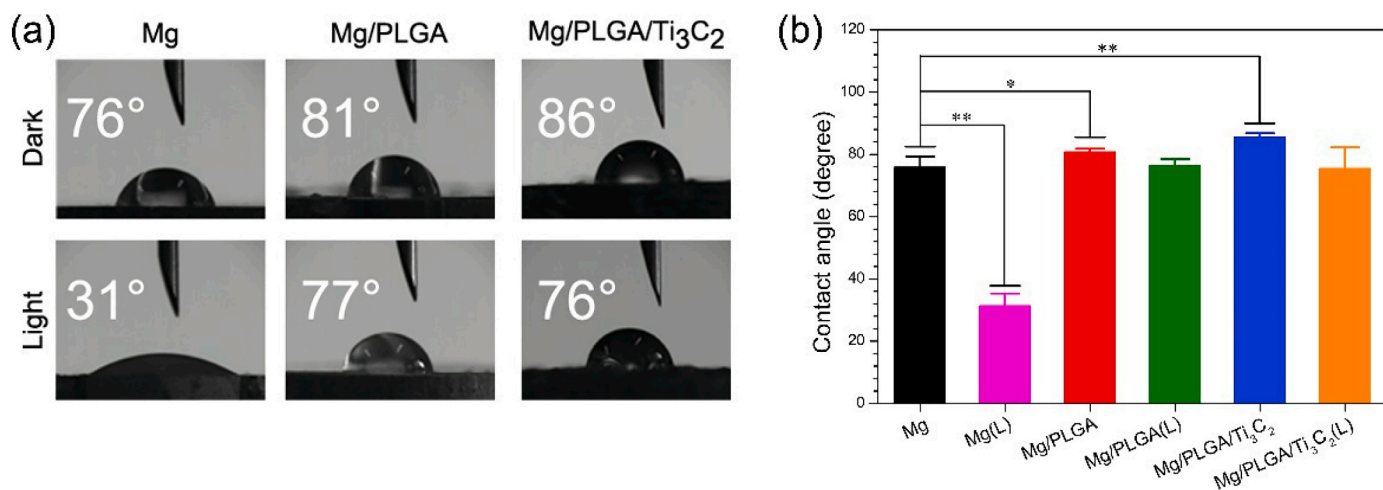


Fig. 9. (a) Optical images of Water contact angle of the different samples; (b) Statistical graph of the water contact angles. (n = 3, mean ± SD, p* < 0.05, p** < 0.01, p*** < 0.001).

PLGA/Ti₃C₂ coating [47]. This phenomenon loosened the stacked Ti₃C₂ nanosheets in the PLGA, and it increased the permeability of the coating to electrolytes. In this case, the conductivity of the Ti₃C₂ nanosheets induced the opposite effect and aggravated the corrosion process [49].

3.4. In vitro cytocompatibility studies

The desired outcome in terms of the biocompatibility of the tissue engineering materials was that the surface of the materials should promote the growth and migration of cells and the adherence of tissues. An important criterion in enhancing biocompatibility is improved wettability. Normally, biomaterials with a moderate surface wetting (35°–80°) are the most suitable for cell growth and adhesion [32]. The water droplets on the surface of the modified samples were documented through optical photographic recording (Fig. 9a). The contact angle values are presented in Fig. 9b. The contact angle of Mg was approximately 76°. Compared with the contact angle of Mg, that of Mg(L) was significantly reduced (31°), indicating that after irradiation with 808 nm NIR laser, the surface hydrophilicity of Mg was improved. This result is mainly attributed to the existence of Cl⁻ ions that formed serious pitting corrosion on Mg due to the irradiation at 808 nm. This roughened structure was conducive for improving the surface wettability of the substrates. Furthermore, the contact angles of Mg/PLGA and Mg/PLGA/Ti₃C₂ were approximately 81° and 86°, respectively. After irradiation, the contact angle of Mg/PLGA(L) and Mg/PLGA/Ti₃C₂(L) were 77° and 76°, respectively. In Mg/PLGA/Ti₃C₂(L), the 808 nm NIR laser irradiation enhanced the water permeability and the surface roughness of the PLGA/Ti₃C₂ hybrid coating; this finding is attributed to the photothermal temperature that exceeded the glass transition temperature (T_g) of the PLGA [46]. Overall, the hybrid coating was conducive for cell growth and adhesion.

Implantable biomaterials must display a good biocompatibility so they can perform their function. The biocompatibility of the modified samples was determined by MTT and cell morphology analyses, and their corresponding cytotoxicity grade was based on the ISO 10993-5. Fig. 10a shows the cell viability test results after culturing by the extracted solution of the different modified samples without 808 nm NIR laser irradiation for 1, 3 and 5 days, respectively. The cell viability result for Mg was basically maintained at approximately 80%, whereas the results for Mg/PLGA and Mg/PLGA/Ti₃C₂ were always higher than 90%. All of the samples showed a grade 1 cytotoxicity, indicating their acceptable biosafety level. Overall, the cell viability results for the three groups did not significantly change with culture time. However, unlike in Mg/PLGA and Mg/PLGA/Ti₃C₂, a significant change in cell viability was observed in Mg after 5 days of incubation. This finding is mainly

attributed to the rapid corrosion rate of Mg in the extraction medium, leading to the extortionate pH values and Mg ion content, which affected the growth and proliferation of the cells. This phenomenon, however, was avoided through modification with PLGA or PLGA/Ti₃C₂, as seen in Mg/PLGA and Mg/PLGA/Ti₃C₂. The results are consistent with the electrochemical and immersion test results.

Fig. 10b shows that compared with the cell viability in Mg, that in Mg(L) decreased significantly to as low as 60% (grade 2 cytotoxicity) after 5 days of culture. However, despite this slight decreased viability in Mg/PLGA(L) and Mg/PLGA/Ti₃C₂(L), the cell viability remained to be at least 85% (grade 1 cytotoxicity). This result suggested that the irradiation with NIR at 808 nm did not significantly alter the cell viability results for Mg/PLGA(L) and Mg/PLGA/Ti₃C₂(L). This finding is consistent with the immersion measurements, indicating that the NIR 808 nm irradiation would not affect the corrosion rate of Mg/PLGA. Moreover, the pH values of Mg/PLGA/Ti₃C₂ increased slowly after irradiation. As a result, the pH values and composition of the culture medium did not dramatically change within a short period of time and thus did not exert a great impact on the cells.

The fluorescent morphologies of the osteoblasts on the surface of the samples are shown in Fig. 10c. Without NIR 808 laser irradiation, a few osteoblasts were observed on the Mg's surface, and they displayed a poor adhesion extension. On the surface of Mg/PLGA, the number of osteoblasts significantly increased and showed an improved spreading morphology. The highest number of osteoblasts and the best spreading morphology were observed on the Mg/PLGA/Ti₃C₂'s surface. The excessive corrosion rate in pure Mg alloys promoted a high concentration of Mg ions, local hydrogen evolution, and over-alkalinization of the culture medium, which was not conducive to cell growth and adhesion. On the contrary, modification with the PLGA/Ti₃C₂ hybrid coating not only improved the anti-corrosion performance of the substrate but also provided a more conducive environment to growth and adhesion of the cells. After irradiating with NIR 808 laser, the number of osteoblasts on the surface of Mg(L) slightly decreased, and the adhesion morphology worsened. By contrast, no significant difference in terms of these parameters was observed between Mg/PLGA(L) and Mg/PLGA. Compared with the number of osteoblasts in Mg/PLGA/Ti₃C₂, that in Mg/PLGA/Ti₃C₂(L) was slightly lower, although the growth condition of cells in these samples was still better than that in the Mg and was similar to that in Mg/PLGA. These results are consistent with MTT measurements.

4. Conclusion

This study is the first to report that the degradation rate of Mg-Sr

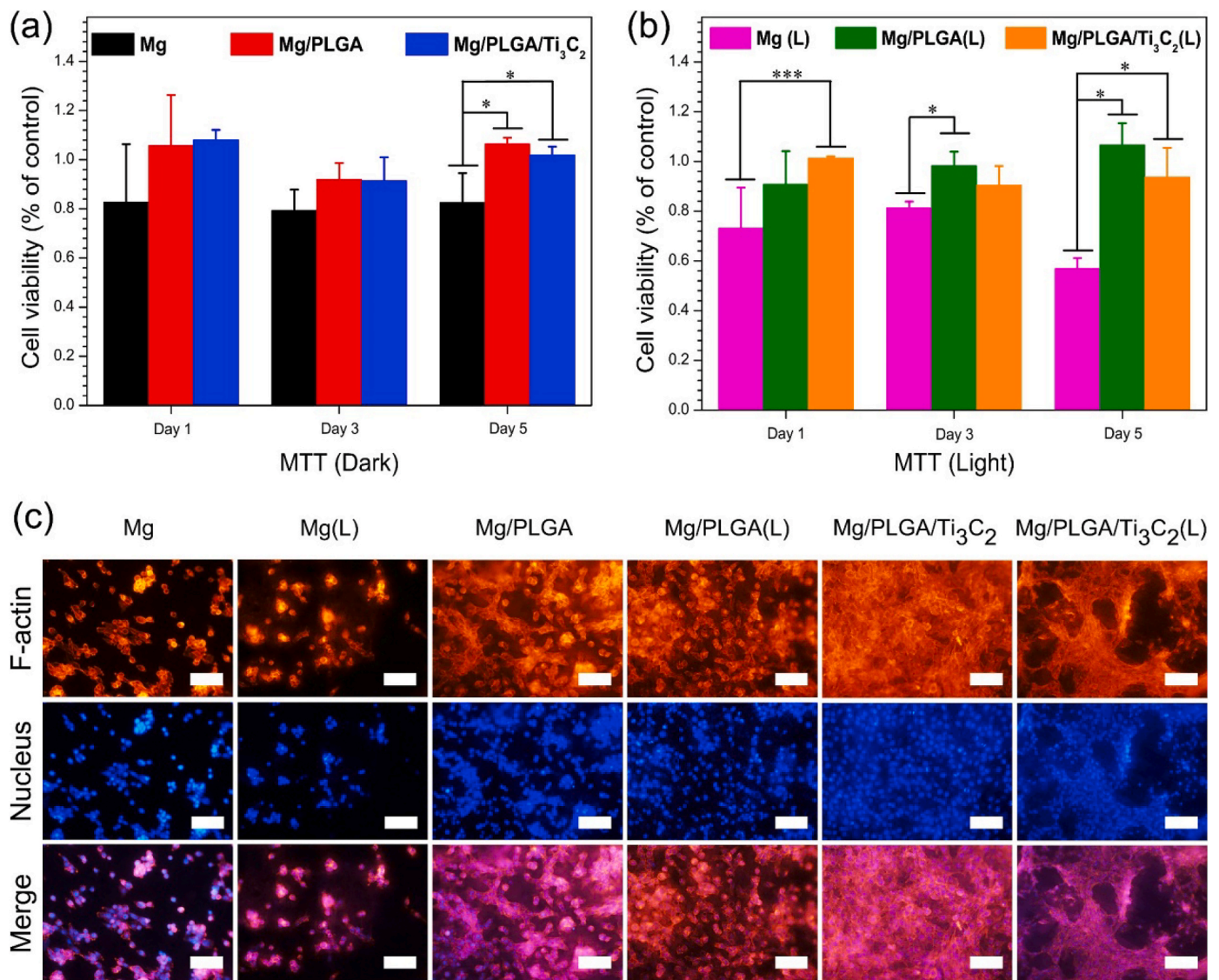


Fig. 10. Cells viability of each group for 1, 3, and 5 days: (a) The extracted solution was cultured in the dark (The corresponding day's control is used as the baseline); (b) The extracted solution was irradiated by NIR 808 nm laser for 20 min. (c) Fluorescence morphologies of cells on different samples (Scale bar = 50 μ m). ($n = 3$, mean \pm SD, $p^* < 0.05$, $p^{**} < 0.01$, $p^{***} < 0.001$).

alloys was successfully regulated by irradiation with 808 nm NIR laser. The results of the electrochemical measurements demonstrated that the i_{corr} values of Mg/PLGA/Ti₃C₂ (7.65×10^{-9} A/cm²) is lower by approximately four orders of magnitude than that of pure Mg-Sr alloy (7.13×10^{-4} A/cm²) in the absence of 808 nm NIR laser irradiation. After irradiation, the i_{corr} value of Mg/PLGA/Ti₃C₂(L) was 3.48×10^{-7} A/cm², an increase by approximately two orders of magnitude relative to that of Mg/PLGA/Ti₃C₂. This finding indicates that the NIR 808 nm laser could regulate the anti-corrosion performance of Mg/PLGA/Ti₃C₂. The immersion results further demonstrated that the PLGA/Ti₃C₂ hybrid coating not only could significantly increase the anti-corrosion performance of the Mg-Sr alloys but could also adjust the corrosion resistance through 808 nm NIR laser irradiation. The results of the cytotoxicity study showed that the presence of PLGA/Ti₃C₂ hybrid coating endowed the Mg-Sr alloy substrates with an enhanced biocompatibility. In conclusion, the idea of constructing biological materials for scaffolds and implants with controllable corrosion resistance and enhanced biocompatibility has just been expanded. This work provides a broader application prospect for biodegradable implant materials.

CRediT authorship contribution statement

Li Liu: Conceptualization, Methodology, Data curation, Writing - original draft. **Bo Huang:** Methodology, Writing - original draft. **Xiangmei Liu:** Conceptualization, Writing - review & editing, Supervision, Project administration. **Wei Yuan:** Methodology, Data curation. **Yufeng Zheng:** Conceptualization, Supervision, Project administration. **Zhaoyang Li:** Methodology. **Kelvin Wai Kwok Yeung:** Methodology. **Shengli Zhu:** Methodology. **Yanqin Liang:** Methodology. **Zhenduo Cui:** Methodology. **Shuilin Wu:** Conceptualization, Writing - review & editing, Supervision, Project administration.

Declaration of competing interest

The authors declare that they have no competing interests.

Acknowledgements

This study was jointly supported by the Natural Science Fund of

Hubei Province no. 2018CFA064, the National Science Fund for Distinguished Young Scholars no. 51925104, the National Natural Science Foundation of China grant nos. 51671081 and 51871162, Hong Kong ITC (ITS/287/17, GHX/002/14SZ), and Health and Medical Research Fund (No. 03142446).

Appendix A. Supplementary data

Supplementary data to this article can be found online at <https://doi.org/10.1016/j.bioactmat.2020.08.013>.

References

- [1] Y. Liu, Y. Zheng, X. Chen, J. Yang, H. Pan, D. Chen, L. Wang, J. Zhang, D. Zhu, S. Wu, K. Yeung, R. Zeng, Y. Han, S. Guan, Fundamental theory of biodegradable metals-definition, criteria, and design, *Adv. Funct. Mater.* 29 (2019) 1805402.
- [2] Y. Zheng, X. Gu, F. Witte, Biodegradable metals, *Mater. Sci. Eng. R* 77 (2014) 1–34.
- [3] S. Wu, X. Liu, K. Yeung, C. Liu, X. Yang, Biomimetic porous scaffolds for bone tissue engineering, *Mater. Sci. Eng. R* 80 (2014) 1–36.
- [4] Y. Yang, C. Lu, S. Peng, L. Shen, D. Wang, F. Qi, C. Shuai, Laser additive manufacturing of Mg-based composite with improved degradation behaviour, *Virtual Phys. Prototyp.* 15 (2020) 278–293.
- [5] Y. Yang, C. He, W. Yang, F. Qi, D. Xie, L. Shen, S. Peng, C. Shuai, Mg bone implant features, developments and perspective, *Mater. Des.* 185 (2020) 108259.
- [6] S. Shadanbaz, G. Dias, Calcium phosphate coatings on magnesium alloys for biomedical applications: a review, *Acta Biomater.* 8 (2012) 20–30.
- [7] Q. Yang, W. Yuan, X. Liu, Y. Zheng, Z. Cui, X. Yang, H. Pan, S. Wu, Atomic layer deposited ZrO₂ nanofilm on Mg-Sr alloy for enhanced corrosion resistance and biocompatibility, *Acta Biomater.* 58 (2017) 515–526.
- [8] J. Chen, M. Gao, L. Tan, K. Yang, Microstructure, mechanical and biodegradable properties of a Mg-2Zn-1Gd-0.5Zr alloy with different solution treatments, *Rare Met.* 38 (2019) 532–542.
- [9] M. Bornapour, N. Muja, D. Shum-Tim, M. Cerruti, M. Pegguleryuz, Biocompatibility and biodegradability of Mg-Sr alloys: the formation of Sr-substituted hydroxyapatite, *Acta Biomater.* 9 (2013) 5319–5330.
- [10] H. Brar, J. Wong, M. Manuel, Investigation of the mechanical and degradation properties of Mg-Sr and Mg-Zn-Sr alloys for use as potential biodegradable implant materials, *J. Mech. Behav. Biomed. Mater.* 7 (2012) 87–95.
- [11] P. Marie, Strontium ranelate: a physiological approach for optimizing bone formation and resorption, *Bone* 38 (2006) S10–S14.
- [12] X. Gu, X. Xie, N. Li, Y. Zheng, L. Qin, *In vitro* and *in vivo* studies on a Mg-Sr binary alloy system developed as a new kind of biodegradable metal, *Acta Biomater.* 8 (2012) 2360–2374.
- [13] R. Suganthi, K. Elayaraja, M. Joshy, V. Chandra, E. Girija, S. Kalkura, Fibrous growth of strontium substituted hydroxyapatite and its drug release, *Mater. Sci. Eng. C* 31 (2011) 593–599.
- [14] X. Zeng, Y. Wang, W. Ding, A. Luo, A. Sachdev, Effect of strontium on the microstructure, mechanical properties, and fracture behavior of AZ31 magnesium alloy, *Metall. Mater. Trans. A* 37 (2006) 1333–1341.
- [15] H. Pan, K. Pang, F. Cui, F. Ge, C. Man, X. Wang, Z. Cui, Effect of alloyed Sr on the microstructure and corrosion behavior of biodegradable Mg-Zn-Mn alloy in Hank's solution, *Corrosion Sci.* 157 (2019) 420–437.
- [16] W. Peng, J. Chen, X. Shan, Y. Wang, F. He, X. Wang, L. Tan, K. Yang, Mg-based absorbable membrane for guided bone regeneration (GBR): a pilot study, *Rare Met.* 38 (2019) 577–587.
- [17] S. Liu, D. Kenta, N. Doan, M. Dargusch, G. Wang, Effects of deformation twinning on the mechanical properties of biodegradable Zn-Mg alloys, *Bioact. Mater.* 4 (2019) 8–16.
- [18] A. Carangelo, A. Acquesta, T. Monetta, *In-vitro* corrosion of AZ31 magnesium alloys by using a polydopamine coating, *Bioact. Mater.* 4 (2019) 71–78.
- [19] Z. Zhen, T. Xi, Y. Zheng, A review on *in vitro* corrosion performance test of biodegradable metallic materials, *Trans. Nonferrous Metals Soc. China* 23 (2013) 2283–2293.
- [20] L. Huang, K. Su, Y. Zheng, K. Yeung, X. Liu, Construction of TiO₂/silane nanofilm on AZ31 magnesium alloy for controlled degradability and enhanced biocompatibility, *Rare Met.* 38 (2019) 588–600.
- [21] Y. Zou, W. Jian, L. Cui, R. Zeng, Q. Wang, Q. Han, J. Qiu, X. Chen, D. Chen, S. Guan, Y. Zheng, Corrosion resistance and antibacterial activity of zinc-loaded montmorillonite coatings on biodegradable magnesium alloy AZ31, *Acta Biomater.* 98 (2019) 196–214.
- [22] X. Li, X. Liu, S. Wu, K. Yeung, Y. Zheng, P. Chu, Design of magnesium alloys with controllable degradation for biomedical implants: from bulk to surface, *Acta Biomater.* 45 (2016) 2–30.
- [23] F. Witte, N. Hort, C. Vogt, S. Cohen, K.U. Kainer, R. Willumeit, F. Feyerabend, Degradable biomaterials based on magnesium corrosion, *Curr. Opin. Solid State Mater. Sci.* 12 (2008) 63–72.
- [24] L. Li, L. Cui, R. Zeng, S. Li, X. Chen, Y. Zheng, M. Kannan, Advances in functionalized polymer coatings on biodegradable magnesium alloys - a review, *Acta Biomater.* 79 (2018) 23–36.
- [25] D. Jiang, X. Xia, J. Hou, G. Cai, X. Zhang, Z. Dong, A novel coating system with self-reparable slippery surface and active corrosion inhibition for reliable protection of Mg alloy, *Chem. Eng. J.* 373 (2019) 285–297.
- [26] A. Nazeer, E. Al-Hetlani, M. Amin, T. Quiñones-Ruiz, I. Lednev, A poly (butyl methacrylate)/graphene oxide/TiO₂ nanocomposite coating with superior corrosion protection for AZ31 alloy in chloride solution, *Chem. Eng. J.* 361 (2019) 485–498.
- [27] Q. Zheng, J. Li, W. Yuan, X. Liu, L. Tan, Y. Zheng, K. Yeung, S. Wu, Metal organic framework incorporated polycaprolactone film for enhanced corrosion resistance and biocompatibility of Mg alloy, *ACS Sustain. Chem. Eng.* 7 (2019) 18114–18124.
- [28] X. Liu, Q. Yang, Z. Li, W. Yuan, Y. Zheng, Z. Cui, X. Yang, K. Yeung, S. Wu, A combined coating strategy based on atomic layer deposition for enhancement of corrosion resistance of AZ31 magnesium alloy, *Appl. Surf. Sci.* 434 (2018) 1101–1111.
- [29] Z. Hu, R. Liu, S. Kairy, X. Li, H. Yan, N. Birbilis, Effect of Sm additions on the microstructure and corrosion behavior of magnesium alloy AZ91, *Corrosion Sci.* 149 (2019) 144–152.
- [30] R. Zeng, W. Qi, H. Cui, F. Zhang, S. Li, E. Han, *In vitro* corrosion of as-extruded Mg-Ca alloys—the influence of Ca concentration, *Corrosion Sci.* 96 (2015) 23–31.
- [31] M. Yamasaki, S. Izumi, Y. Kawamura, H. Habazaki, Corrosion and passivation behavior of Mg-Zn-Y-Al alloys prepared by cooling rate-controlled solidification, *Appl. Surf. Sci.* 257 (2011) 8258–8267.
- [32] H. Qi, S. Heise, J. Zhou, K. Schuhladden, Y. Yang, N. Cui, R. Dong, S. Virtanen, Q. Chen, A. Boccacini, T. Lu, Electrophoretic deposition of bioadaptive drug delivery coatings on magnesium alloy for bone repair, *ACS Appl. Mater. Interfaces* 11 (2019) 8625–8634.
- [33] M. Ghidui, M. Lukatskaya, M. Zhao, Y. Gogotsi, M. Barsoum, Conductive two-dimensional titanium carbide 'clay' with high volumetric capacitance, *Nature* 516 (2014) 78–81.
- [34] M. Naguib, M. Kurtoglu, V. Presser, J. Lu, J. Niu, M. Heon, L. Hultman, Y. Gogotsi, M. Barsoum, Two-dimensional nanocrystals produced by exfoliation of Ti₃AlC₂, *Adv. Mater.* 23 (2011) 4248–4253.
- [35] W. Bao, C. Shuck, W. Zhang, X. Guo, Y. Gogotsi, G. Wang, Boosting performance of Na-S batteries using sulfur-doped Ti₃C₂T_x MXene nanosheets with a strong affinity to sodium polysulfides, *ACS Nano* 13 (2019) 11500–11509.
- [36] M. Lukatskaya, O. Mashtalir, C. Ren, Y. Dall'Agnese, P. Rozier, P. Taberna, M. Naguib, P. Simon, M. Barsoum, Y. Gogotsi, Cation intercalation and high volumetric capacitance of two-dimensional titanium carbide, *Science* 341 (2013) 1502–1505.
- [37] W. Tang, Z. Dong, R. Zhang, X. Yi, K. Yang, M. Jin, C. Yuan, Z. Xiao, Z. Liu, L. Cheng, Multifunctional two-dimensional core-shell MXene@Gold nanocomposites for enhanced photo-radio combined therapy in the second biological window, *ACS Nano* 13 (2019) 284–294.
- [38] J. Xuan, Z. Wang, Y. Chen, D. Liang, L. Cheng, X. Yang, Z. Liu, R. Ma, T. Sasaki, F. Geng, Organic-base-driven intercalation and delamination for the production of functionalized titanium carbide nanosheets with superior photothermal therapeutic performance, *Angew. Chem. Int. Ed.* 55 (2016) 14569–14574.
- [39] Q. Xue, H. Zhang, M. Zhu, Z. Pei, H. Li, Z. Wang, Y. Huang, Y. Huang, Q. Deng, J. Zhou, S. Du, Q. Huang, C. Zhi, Photoluminescent Ti₃C₂ MXene quantum dots for multicolor cellular imaging, *Adv. Mater.* 29 (2017) 1604847.
- [40] G. Liu, J. Zou, Q. Tang, X. Yang, Y. Zhang, Q. Zhang, W. Huang, P. Chen, J. Shao, X. Dong, Surface modified Ti₃C₂ MXene nanosheets for tumor targeting photothermal/photodynamic/chemo synergistic therapy, *ACS Appl. Mater. Interfaces* 9 (2017) 40077–40086.
- [41] Z. Yuan, P. Wei, Y. Huang, W. Zhang, F. Chen, X. Zhang, J. Mao, D. Chen, Q. Cai, X. Yang, Injectable PLGA microspheres with tunable magnesium ion release for promoting bone regeneration, *Acta Biomater.* 85 (2019) 294–309.
- [42] L. Chen, Y. Sheng, H. Zhou, Z. Li, X. Wang, W. Li, Influence of a MAO + PLGA coating on biocorrosion and stress corrosion cracking behavior of a magnesium alloy in a physiological environment, *Corrosion Sci.* 148 (2019) 134–143.
- [43] M. Yu, L. Xu, F. Tian, Q. Su, N. Zheng, Y. Yang, J. Wang, A. Wang, C. Zhu, S.Y. Guo, X. Zhang, Y. Gan, X. Shi, H. Gao, Rapid transport of deformation-tuned nanoparticles across biological hydrogels and cellular barriers, *Nat. Commun.* 9 (2018) 2607.
- [44] N. Ostrowski, B. Lee, A. Roy, M. Ramanathan, P. Kumta, Biodegradable poly(lactide-co-glycolide) coatings on magnesium alloys for orthopedic applications, *J. Mater. Sci. Mater. Med.* 24 (2013) 85–96.
- [45] L. Liu, Q. Yang, L. Huang, X. Liu, Y. Liang, Z. Cui, X. Yang, S. Zhu, Z. Li, Y. Zheng, K. Yeung, S. Wu, The effects of a phytic acid/calcium ion conversion coating on the corrosion behavior and osteoinductivity of a magnesium-strontium alloy, *Appl. Surf. Sci.* 484 (2019) 511–523.
- [46] S. Shah, Y. Cha, C. Pitt, Poly (glycolic acid-co-DL-lactic acid): diffusion or degradation controlled drug delivery? *J. Contr. Release* 18 (1992) 261–270.
- [47] J. Choi, H. Seo, J. Park, J. Son, D. Kim, J. Kim, G. Moon, D. Hyun, Poly(D,L-lactic-co-glycolic acid) (PLGA) hollow fiber with segmental switchability of its chains sensitive to NIR light for synergistic cancer therapy, *Colloids Surf., B* 173 (2019) 258–265.
- [48] G. Baril, G. Galicia, C. Deslouis, N. Pèbère, B. Tribollet, V. Vivier, An impedance investigation of the mechanism of pure magnesium corrosion in sodium sulfate solutions, *J. Electrochem. Soc.* 154 (2007) C108–C113.
- [49] S. De, J. Lutkenhaus, Corrosion behaviour of eco-friendly airbrushed reduced graphene oxide-poly(vinyl alcohol) coatings, *Green Chem.* 20 (2018) 506–514.
- [50] H. Zhou, R. Chen, Q. Liu, J. Liu, J. Yu, C. Wang, M. Zhang, P. Liu, J. Wang, Fabrication of ZnO/epoxy resin superhydrophobic coating on AZ31 magnesium alloy, *Chem. Eng. J.* 368 (2019) 261–272.